ACS Catalysis

pubs.acs.org/acscatalysis

Research Article

Controlling the Oxidation State of Fe-Based Catalysts through Nitrogen Doping toward the Hydrodeoxygenation of *m*-Cresol

Yanling Yang, Mingwu Tan, Aidan Garcia, Zhaoxia Zhang, Jingdong Lin, Shaolong Wan, Jean-Sabin McEwen, Shuai Wang,* and Yong Wang*

Cite This: *ACS Catal.* 2020, 10, 7884−7893

Read Online

ACCESS | Metrics & More | Article Recommendations | Supporting Information

ABSTRACT: Stabilizing the oxidation state of Fe is of great importance for the rational design of Fe-based catalysts. To this end, N-doped carbon composites (NC) are prepared with different N-doping contents and used as supports for Fe particles. We find N-doped carbonaceous materials enable an effective control of the Fe oxidation state via an electronic interaction between Fe and N. This interaction leads to a decrease in the Fe particle size when the N-doping content is increased, as shown by structural characterization of transmission electron microscopy and powder X-ray diffraction, and to a weakened oxygen affinity of the Fe particles in the presence of N-doped sites, as unveiled by H_2-temperature-programmed reduction measurements with separate N_2O and water vapor pretreatments. The weaker oxygen affinity correlates with the excellent long-term stability of Fe/NC catalysts during the hydrodeoxygenation of lignin-derived *m*-cresol to form valuable aromatic products, whereas obvious oxidative deactivation is observed for Fe/C. An investigation of the surface nitrogen composition of all N-doped samples shows that their deactivation rate constants are closely related to the nitrogen content anchoring Fe into the carbon architecture, which indicates unambiguously that embedding nitrogen into the carbon skeleton (mainly including pyridinic and pyrrolic nitrogen functional groups) plays a critical role in stabilizing Fe, while amino-N is inclined to suffering from wastage during the hydrodeoxygenation reaction. These results are further confirmed computationally through an electronic analysis of Fe−N complexes embedded into graphene, showing that skeletal nitrogen sites shield Fe from oxidation relative to bare carbon or aminic nitrogen.

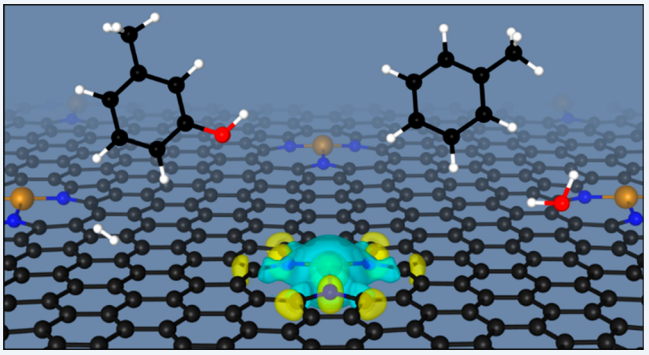

KEYWORDS: *N-doped carbonaceous materials, oxygen affinity, Fe-based catalysts, catalytic stability, hydrodeoxygenation, biomass conversion*

Downloaded via WASHINGTON STATE UNIV on August 27, 2020 at 17:56:59 (UTC).
See https://pubs.acs.org/sharingguidelines for options on how to legitimately share published articles.

1. INTRODUCTION

The high oxygen content of biomass is a crucial hurdle in the upgrading of such renewable carbon resources into useful fuels and chemicals.[1−5] Hydrodeoxygenation provides an essential way to remove oxygen from biomass feedstocks as the form of H_2O,[6−8] and Fe-based catalysts show great promise for this application (especially for lignin-derived compounds) due to their low cost and high selectivity of C−O hydrogenolysis over C−C hydrogenolysis or C═C hydrogenation.[9−12] However, Fe-based catalysts usually suffer severe deactivation during a hydrodeoxygenation reaction, resulting from the oxidation of metallic Fe by H_2O formed in situ or contained in the biomass-derived reactant feed at high-temperature reaction conditions.[13] Improving the resistance of these promising catalysts with regard to oxidation remains a key challenge to the rational development of novel Fe-based catalysts for biomass conversion.

Doping of a noble metal is a widely studied strategy to enhance the antioxidant ability of Fe-based catalysts.[9,14,15] Our recent report indicates that the presence of a noble metal facilitates the removal of surface O-containing species on Fe surfaces via the formation of spillover H adatoms from fast H_2 dissociation on the noble metal sites.[15] The high cost of the noble metal may, however, hinder the application of this strategy in practical biomass upgrading. Exploring new strategies to efficiently protect Fe-based catalysts from oxidation during catalysis is thus still highly desired.

Nitrogen-doped carbon materials have been found as an appropriate support for Fe-based catalysts.[16−18] The interaction between the Fe particles and the doped N sites helps to anchor and disperse the Fe particles.[19−22] A recent K-edge

Received: February 5, 2020
Revised: April 14, 2020
Published: May 18, 2020

© 2020 American Chemical Society

https://dx.doi.org/10.1021/acscatal.0c00626
ACS Catal. 2020, 10, 7884−7893

XANES analysis of Fe in Fe-based catalysts supported on N-doped graphene has reported a decrease in the peak intensity as compared to the samples where only Fe is incorporated into the carbonaceous framework.[22] From these observations, the authors concluded that N is able to increase the electron density of the Fe particles. However, such an analysis implicitly assumes that the XANES spectra is a fingerprint of the oxidation state of Fe, which we have recently demonstrated may not be the case since it also depends sensitively on the ligand environment of the complex.[23,24]

In this work, we show that this mediation of the electronic state by the Fe−N interaction allows us to control the oxidation state of Fe catalysts with a moderate doping amount of N, rendering such modified catalysts to remain highly stable during the hydrodeoxygenation of *m*-cresol (a representative lignin derivative). Combined experimental and theoretical assessments further discern the roles of various surface N species, such as pyridinic-N, pyrrolic-N, and amino-N moieties, on the stabilization of Fe-based catalysts. It is unveiled that pyrrolic and pyridinic N species alter the oxidation state of Fe by decreasing its electron density and making it stable toward the hydrodeoxygenation of *m*-cresol. These new findings would bring a basis to the rational design of novel Fe-based catalysts with inexpensive and tunable N-doped carbon supports.

2. METHODS

2.1. Catalyst Preparation. N-doped carbon supports were prepared using a template method as described elsewhere.[25] Glucose (Macklin, China, >99%), D-glucosamine hydrochloride (denoted as GAH; Macklin, China, >99%), and MgO (Sinopharm Chemical Reagent Co., China, >99.9%) were chosen as the carbon source, nitrogen source, and parent template, respectively. The total amount of GAH and glucose was kept at 5.0 g, while their mass ratio was varied to obtain different N-doped contents (from 2.0% to 7.8% in mass). These mixtures were dissolved in deionized water (100 mL) in a crucible, and MgO powder (1.3 g) was added into this solution under stirring. The crucible was then heated in an oil bath at 150 °C to evaporate water, and the resulting dark brown solid was further heated to 550 °C with a ramp rate of 10 °C min^{-1} in flowing N_2 (400 mL min^{-1}) and held at 550 °C for 1 h. After cooling to room temperature, the sample was dissolved in an excess dilute HCl aqueous solution over 24 h to remove the MgO template, and then filtered and washed with deionized water several times until the pH value of the filtrate approached around 7.0. The obtained solid was dried at 60 °C overnight to obtain N-doped carbon supports (denoted as NC-*x*, in which *x* stands for the N content in mass).

N-doped carbon supported Fe catalysts (denoted as Fe/NC-*x*) were prepared by an impregnation method. Using the synthesis of 5 wt % Fe/NC-*x* as an example, 1.0 g NC-*x* power and 0.38 g $Fe(NO_3)_3{\cdot}9H_2O$ were dispersed together with deionized water (20 mL) under ultrasonic treatment for 1 h. The mixture was transferred into a drying oven and treated at 60 °C overnight, followed by heating to 450 °C (5 °C min^{-1}) and holding at 450 °C for 2 h in flowing N_2 of 50 mL min^{-1}. Before any characterization or catalytic test, these samples were prereduced in a flow of 50% H_2/N_2 (50 mL min^{-1}) at 350 °C for 3 h.

2.2. Catalyst Characterization. Powder X-ray diffraction (XRD) patterns of solid samples were obtained using a Panalytical X'pert PRO diffractometer (Philips, Netherlands) with the Cu Kα radiation (λ = 0.15406 nm) at a voltage of 40 kV and a current of 30 mA. The contents of N and C elements for these samples were analyzed using the Vario EL III gas-phase elemental analyzer (Elementar, Germany) in O_2 atmosphere (0.25 MPa).

The morphology of Fe/NC-*x* was examined both on the Supra 55 field emission scanning electron microscope (SEM; Zeiss, Germany) operating at 10 kV and on the Tecnai G2 F20 transmission electron microscope (TEM; FEI, U.S.) operating at 200 kV. Size distributions of the Fe particles were analyzed by counting over 100 Fe particles in the TEM images for each sample.

H_2-temperature-programmed reduction (H_2-TPR) of Fe/NC-*x* catalysts with N_2O pretreatment was carried out in a homemade fixed-bed reactor in order to study the interaction between the carbon-based supports and the Fe particles. 100 mg of the catalyst sample was placed in the center of the quartz reactor plugged with ceramic wool and pretreated in a flow of 50% H_2/N_2 (50 mL min^{-1}) at 450 °C for 2 h and cooled to 80 °C in an N_2 atmosphere, followed by a treatment in flowing 5% N_2O/N_2 (50 mL min^{-1}) at 80 °C for 1 h. H_2-TPR experiments were then conducted by heating the sample from 30 to 800 °C (10 °C min^{-1}) in flowing 5% H_2/Ar (30 mL min^{-1}). The H_2 uptake was measured and quantified using both of a thermal conductivity detector (TCD) and a mass spectrometer (Header, U.S.A.).

An X-ray photoelectron spectroscopy (XPS) analysis was performed on a Quantum 2000 scanning ESCA microprobe instrument (Physical Electronics, U.K.) with Al Kα irradiation at 5.0 × 10^{-9} mbar. All binding energy values were referenced to the C 1s signal at 284.4 eV.

2.3. Catalytic Reactions and Product Analysis. Catalytic experiments were carried out in a fixed-bed quartz reactor (internal diameter = 1 cm). The reactor was placed in a temperature-controlled furnace with a K-type thermocouple attached at the center of the catalyst bed outside the quartz tube for measuring reaction temperature, and the vaporizer was maintained at 220 °C. Prior to the tests, the catalyst (60−80 mesh) was heated to 350 °C (5 °C min^{-1}) in a flow of 50% H_2/N_2 (50 mL min^{-1}) and held at 350 °C for 3 h. After purging by flowing N_2 at 350 °C for 0.5 h, *m*-cresol (99%, Sigma-Aldrich) was introduced into the vaporizer using a syringe pump (Core Parmer 74900) and carried into the reactor by a gaseous mixture of H_2 and N_2 with a *m*-cresol partial pressure of 0.5 kPa. All transfer lines were kept at above 220 °C to avoid condensation of liquid reactants or products. The effluent of the reactor was analyzed by an online gas chromatograph (Shimadzu 2800) with a flame ionization detector (FID) and a TCD equipped with RTX-5 (30 m, 0.25 mm i.d. × 0.25 μm) and TDX-01 (3 m, 3 mm i.d. × 2 mm) columns, respectively. The response factors for *m*-cresol and the reaction products were determined using standard compounds. The carbon mass balance of the products, unless otherwise noted, was at least 95%.

2.4. Computational Oxidation Analysis. Favorability of site oxidation was simulated with simplified single-site Fe models using the Vienna ab initio Simulation Package.[26−28] The core electrons were modeled with the projector augmented wave (PAW) method (versions updated in 2012), and a plane-wave basis set with an energy cutoff of 450 eV and the Perdew−Burke−Ernzerhof (PBE) exchange-correlation functional with spin polarization enabled were used to model the valence electrons.[29,30] The Gaussian smearing method was used to set partial occupancies of bands with a

https://dx.doi.org/10.1021/acscatal.0c00626
ACS Catal. 2020, 10, 7884−7893

smearing width of 0.2 eV to facilitate Brillouin zone integration convergence, followed by extrapolation to 0 K for the total energy calculation. Due to the ferromagnetic nature of Fe, the effect of spin polarization was found to be significant and was accounted for in all calculations. The energy tolerance was set to 10^{-5} eV. Nitrogen functionalization was studied in two different graphene models similar to those used in our previous work: a pristine graphene sheet (14.8 × 14.8 × 20 Å) and a graphene nanoribbon with hydrogen terminated edges (29 × 17 × 21 Å).[31] In the graphene nanoribbon model, the layer to layer distance in the supercell is 17 Å, and the graphene lattice constant is 2.467 Å. Illustrations of these models that were used in our calculations are shown in the Supporting Information (SI). The integration of the Brillouin zone was conducted using a (3 × 3 × 1) Monkhorst–Pack[32] grid for pristine graphene, while a (1 × 2 × 3) Monkhorst–Pack grid was used for the graphene nanoribbon models. The optimized lattice constant for bulk Fe was found to be 2.83 Å when the Brillouin zone was sampled with a (20 × 20 × 20) Monkhorst–Pack grid. Calculations for molecules in the gas phase were performed using an 18 × 19 × 20 Å box and one single k-point (the Gamma point) to span the Brillouin zone.

Single-site graphene defects with various types of nitrogen doping (Figure 1a) were modeled with both bare Fe (Figure 1b) and ferrous oxide (Figure 1c) centers. First, bare graphene ribbons were relaxed to a specified force tolerance of 0.02 eV $Å^{-1}$. Single-atom Fe centers were then inserted into the models before a second relaxation. Following the addition of an oxygen atom to the Fe centers, these models were relaxed a final time. Energies from all three stages were collected and compared to those of O_2, H_2, H_2O, and metallic Fe models for reference.

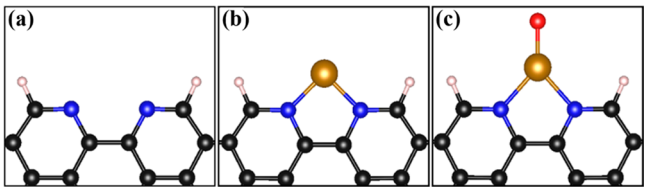

Figure 1. Demonstration of a bare dipyridinic graphene site (a), and those with bound bare Fe (b) and with bound ferrous oxide (c). The gray, blue, brown, red, and white spheres are carbon, nitrogen, iron, oxygen, and hydrogen atoms, respectively.

Using the aforementioned energies, reaction energies for Fe adsorption and subsequent oxidation were calculated. Adsorption energies for the Fe center (E_{ads}) were calculated using the following equation:

$$E_{ads} = E_{Fe_{ads}} - (E_{surf} + E_{Fe_{bulk}}) \quad (1)$$

where $E_{Fe_{ads}}$, E_{Surf}, and $E_{Fe_{bulk}}$ denote the calculated energies for the entire surface-iron structure, the functionalized carbon surface, and the bulk iron, respectively. As the oxidant of concern is water generated during hydrodeoxygenation, the site oxidation energies (E_{Ox}) were calculated using H_2O as the reference reactant:

$$E_{Ox} = (E_{FeO_{ads}} + E_{H_2}) - (E_{Fe_{ads}} + E_{H_2O}) \quad (2)$$

where $E_{FeO_{ads}}$ represents the energy of the oxidized Fe structure, and the other terms represent the energies of their respective reactants and products. These resulting energies were used to assess the favorability of different sites toward the incorporation of Fe into the nitrogen-doped carbonaceous material, as well as the poisoning of the bound Fe with oxygen.

3. RESULTS AND DISCUSSION

3.1. Preparation and Characterization of Nitrogen-Doped Carbon Supports. The NC-*x* supports used in this study were prepared via cocoating of glucose and D-glucosamine hydrochloride (GAH) on the MgO template, followed by calcination in flowing N_2 at high temperature and subsequent removal of the hard template via acid washing (section 2.1). The nitrogen content in these NC-*x* supports was controlled by changing the mass ratio between GAH and glucose. As shown in Figure 2a, XRD patterns of these NC-*x* samples exhibit a general broad diffraction peak centered around 25° only, reflecting their amorphous nature. The absence of diffraction peaks corresponding to MgO phases (e.g., 42.9° and 62.3°) in these XRD patterns indicates the template was removed completely after the acid treatment. SEM and TEM images reveal stacked lamellar structures of these NC-*x* supports (Figures 3a,b, using the NC-3.7 sample as an example), which is derived from the MgO template. Energy-dispersive X-ray spectroscopy (EDS) mapping further confirms that nitrogen distributes uniformly in the carbon nanosheets, whereas the magnesium signal is undetectable (Figure 3c). The stacking of these nanosheets also leads to the formation of mesopores (Figure S1 of the SI), as evidenced by the hysteresis loops formed in the isothermal adsorption–desorption curves of N_2.[33] The pore size of these NC-*x* samples increased gradually from 2.8 to 5.5 nm as the nitrogen content increased from 0 to 7.8% by mass (Table S1 in the SI), in concomitant with a decline of their surface area from 559 to 285 $m^2\ g^{-1}$. These phenomena of the structure change indicate that the introduction of N leads to the collapse of small pores, consistent with the observed fragmentization of the carbon material induced by N-doping.[34] Taken together, the above characterization results show the successful preparation of N-doped carbon nanosheets with tunable nitrogen content and surface area, which were used next as the supports of Fe-based hydrodeoxygenation catalysts.

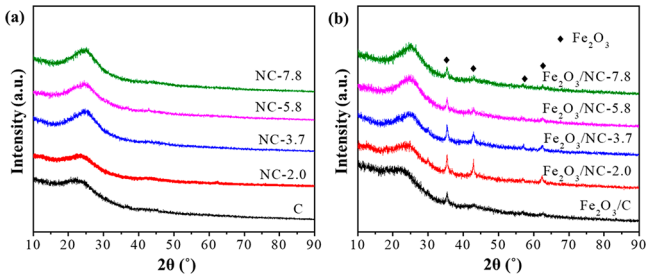

Figure 2. XRD patterns of (a) NC-*x* and (b) Fe_2O_3/NC-*x* samples.

3.2. Structure and Oxygen Affinity of Fe/NC-*x* Catalysts. Five wt % Fe_2O_3/NC-*x* catalysts were prepared via impregnation using $Fe(NO_3)_3$ as the Fe precursor. After thermal treatment of $Fe(NO_3)_3$/NC-*x* in N_2 atmosphtere at 450 °C, the Fe species dispersed by the NC-*x* support showed XRD peaks around 2θ values of 35.4°, 43.0°, 56.7°, and 62.5° (Figure 2b), ascribing to the (311), (400), (511), and (440) planes of cubic Fe_2O_3 (PDF no. 39-0238), respectively.[35] These results indicate the full decomposition of the $Fe(NO_3)_3$ precursor into Fe_2O_3 particles during the high-temperature treatment. The diffraction peaks of the Fe_2O_3 phase for Fe_2O_3/

https://dx.doi.org/10.1021/acscatal.0c00626
ACS Catal. 2020, 10, 7884–7893

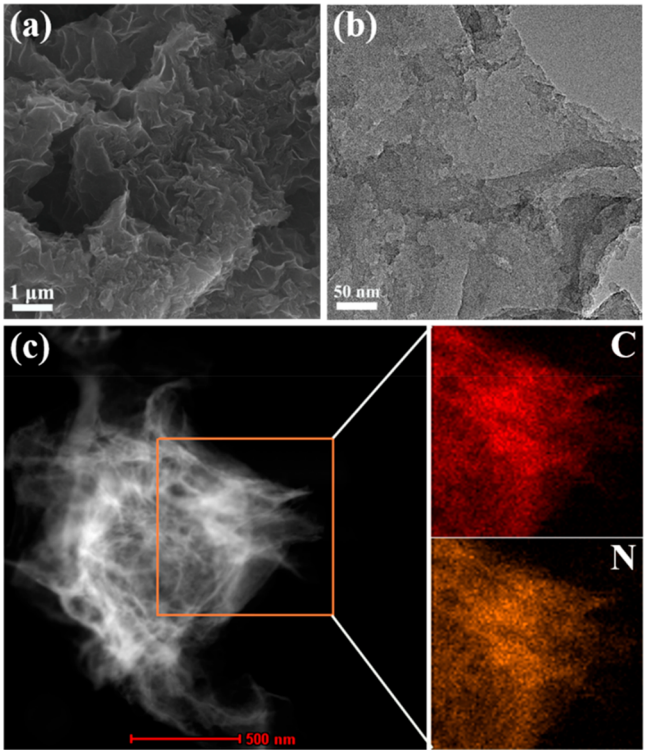

Figure 3. (a) SEM and (b) TEM images of the NC-3.7 sample and (c) HAADF-STEM images of this sample with inserted EDS mapping of C and N elements for the selected region.

NC-*x* became weaker as the N content of the NC-*x* support increased, which corresponds to a decrease of the Fe_2O_3 particle size from 20.9 to 16.8 nm (estimated using the Scherrer equation; Table S2 in the SI). In contrast, Fe_2O_3/C exhibited broader diffraction peaks and thus smaller Fe_2O_3 particles (15.5 nm) as compared to those for the Fe_2O_3/NC-*x* samples. We surmise that, in the absence of N dopants, Fe_2O_3 clusters nucleated and grew uniformly on the carbon support during the decomposition of the $Fe(NO_3)_3$ precursor, but preferred to nucleate at the scarce N sites when occurring on the NC-*x* supports because of the Fe−N interaction,[19] which led to the formation of Fe_2O_3 particles larger than those on the pure carbon support. Consistent with this hypothesis, the size of the Fe_2O_3 particles on NC-*x* decreased with increasing nitrogen content, as a result of the formation of more nitrogen-bound Fe_2O_3 nuclei during the $Fe(NO_3)_3$ decomposition process.

The treatment of these Fe_2O_3/NC-*x* samples in flowing 50% H_2/N_2 at 350 °C fully reduced the Fe_2O_3 particles to metallic Fe, as indicated by the disappearance of the Fe_2O_3 signals and the appearance of those belonging to the Fe phase in their XRD patterns (Figure S2 in the SI). TEM images further showed that the average particle size of the Fe particles in the formed Fe/NC-*x* catalysts decreased from 16.0 to 9.7 nm as the N content increased from 2.0% to 7.8% (in mass), whereas the corresponding average particle size of Fe for the Fe/C sample was 6.9 nm (Figure 4). The trend of the Fe particle size change in these supported Fe catalysts is similar to that for the Fe_2O_3 particles of their oxide precursors (Figure 2b), indicating the effect of N content on the Fe particle size can be traced back to the N-mediated Fe_2O_3 formation via $Fe(NO_3)_3$ decomposition on the NC-*x* supports.

N_2O chemisorption and H_2-temperature-programmed reduction (H_2-TPR) were combined here to determine the oxygen affinity of the exposed Fe surface sites on these Fe/NC-*x* catalysts, which correlates directly to the catalytic activity and stability of Fe particles in hydrodeoxygenation reactions.[36,37] The chemisorption of N_2O on the Fe-based catalysts was performed at a low temperature of 80 °C to ensure that N_2O only oxidized the surface of the Fe particles. The interaction between the adsorbed oxygen and the Fe surface sites (i.e., the oxygen affinity) was then assessed by the temperature required to remove these adsorbed oxygen species via hydrogenation in the subsequent H_2-TPR process.

As shown in Figure 5a, the Fe/C catalyst exhibited an H_2 consumption peak centered at 375 °C after the chemisorption of N_2O, which can be assigned to the reduction of surface FeO_x species formed by the oxidation of N_2O because the reduction temperature is apparently lower than those for the bulk FeO or Fe_2O_3 phases (>400 °C).[15,38,39] For the Fe/NC-*x* samples, the H_2 reduction peaks shift to lower temperatures (340 to 315 °C) as the concentration of the doped nitrogen increases, reflecting how the oxygen affinity of the Fe particles is weakened in the presence of the doped N sites. It is noted that the reduction temperature for the Fe/C catalysts became reversely higher for larger Fe particles (e.g., 385 °C in Figure S3 of the SI for Fe/C catalysts of ∼10 nm Fe particles; the

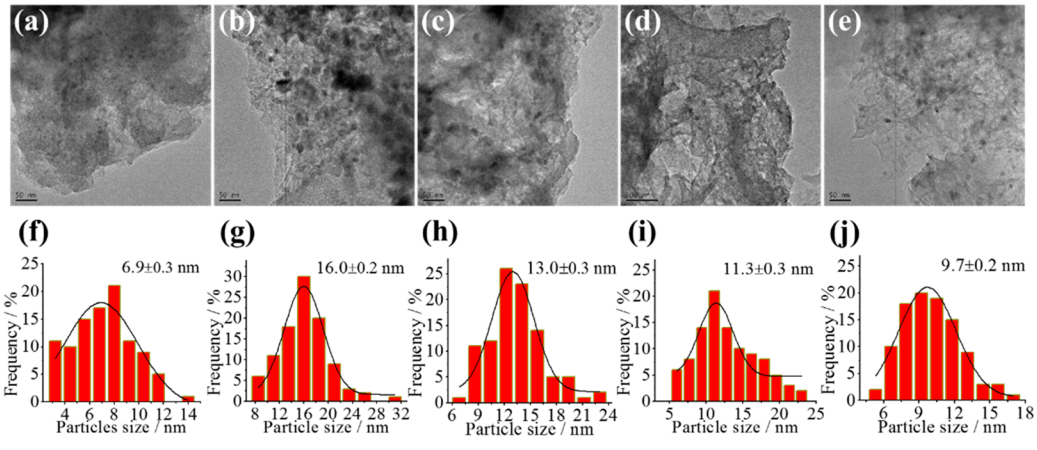

Figure 4. TEM images of (a) Fe/C, (b) Fe/NC-2.0, (c) Fe/NC-3.7, (d) Fe/NC-5.8, and (e) Fe/NC-7.8 with the corresponding statistic Fe particle size distribution bar charts (f−j).

https://dx.doi.org/10.1021/acscatal.0c00626
ACS Catal. 2020, 10, 7884−7893

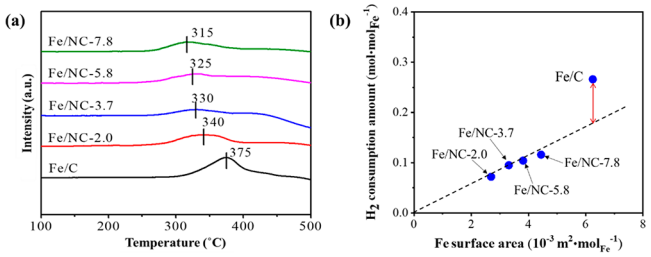

Figure 5. (a) H_2-TPR profiles of Fe/NC-x catalysts after being treated by flowing 5% N_2O/N_2 at 80 °C for 1 h and (b) the relation between the corresponding consumed H_2 amount and the exposed surface area of the Fe particles estimated from the TEM-determined particle size.

TEM image of this sample shown in Figure S4). Therefore, the observed change of the oxygen affinity for these Fe/NC-*x* samples is not ascribed to their larger Fe particle sizes as compared to that of the Fe/C catalyst, but appears to be determined by the interaction of the N site to the Fe particles, which affects the surface electron density of the Fe particles and consequently destabilizes the O^{2-} species bound to the Fe surfaces. Figure 5b further shows that, for Fe/NC-*x* catalysts, a linear correlation exists between the amount of consumed H_2 during the TPR process and the exposed Fe surface area as estimated from the TEM-determined Fe particle sizes (Figure 4), while the H_2 consumption amount of the Fe/C sample is apparently larger than the value predicted from this trend. This observed deviation implies that the Fe particle surface on the Fe/NC-*x* catalysts are more affected by the doping of N as compared to Fe/C, providing additional evidence for the strong interaction between the N species of the carbon support and the Fe particles.

3.3. Stability of Fe/NC-*x* Catalysts in the Hydrodeoxygenation of *m*-Cresol. The influence of nitrogen doping on the stability of Fe/NC-*x* catalysts for hydrodeoxygenation was investigated here using *m*-cresol as the model reactant, which is a representative lignin derivative and has been widely studied. According to previous reports,[13,40] *m*-cresol hydrodeoxygenation on Fe-based catalysts yields toluene via benzene ring-oxygen bond cleavage and phenol via C−C hydrogenolysis, of which the former is generally the main product. Subsequent C−C hydrogenolysis of the methyl group in toluene and alkylation of the aromatic ring with the methyl intermediates form benzene and xylene, respectively (shown in Scheme 1).

Scheme 1. Reaction Pathways of *m*-Cresol Hydrodeoxygenation on Fe-Based Catalysts

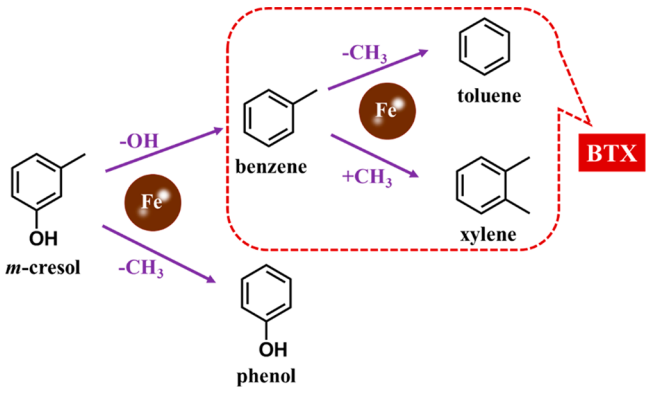

Figure 6a depicts how the Fe/C catalyst suffers severe deactivation in *m*-cresol hydrodeoxygenation at 350 °C (0.5

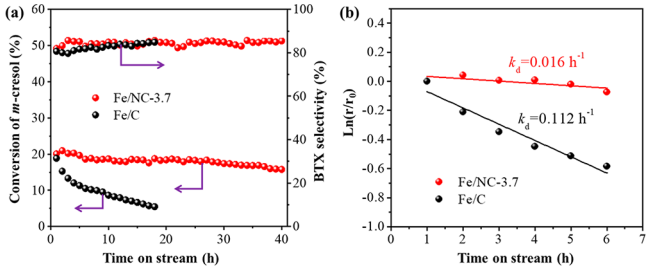

Figure 6. Stability comparison between the Fe/C and Fe/NC-3.7 catalysts in *m*-cresol hydrodeoxygenation at 350 °C: (a) *m*-cresol convrsions and BTX selectivities along time-on-stream and (b) corresponding changes of relative rates with respect to the initial rates (r/r_0). Reaction conditions: 40 mg Fe/C or 150 mg Fe/NC-3.7 to obtain an initial *m*-cresol conversion of ~20%; 0.5 kPa $P_{m\text{-cresol}}$, 40 kPa P_{H_2}, balanced by N_2.

kPa *m*-cresol; 40 kPa P_{H2}). The *m*-cresol conversion decreased from 20% to 7% within a time on stream of 18 h, although the combined selectivities for benzene, toluene, and xylene (denoted as BTX, Scheme 1) are kept nearly constant around 80% (detailed product distribution shown in Table S3 of the SI). In contrast, the N-doping in the carbon support significantly improves the catalytic stability of the Fe particles. For instance, the *m*-cresol conversion on the Fe/NC-3.7 sample decreased merely from 20% to 16% even after the time-on-stream reached 40 h at the same reaction conditions (Figure 6a), in which the BTX selectivity was as high as that for the Fe/C catalyst (detailed product distribution shown in Table S3 of the SI). The deactivation behavior of these supported Fe catalysts in *m*-cresol hydrodeoxygenation followed pseudo-first-order deactivation kinetics (Figure 6b). The regression-fitted deactivation kinetic constants (k_d) for the Fe/C and Fe/NC-3.7 samples were 0.016 and 0.112 h^{-1}, respectively (Figure 6b), revealing that a small amount of nitrogen doping in the carbon support reduces the deactivation rate of Fe particles almost by 1 order of magnitude.

TEM characterization of the spent Fe/C and Fe/NC-3.7 catalysts (Figure S5 of the SI) shows that the Fe particles of these two samples increased their size to a similar extent (less than a factor of 2) during the hydrodeoxygenation of *m*-cresol (i.e., from 6.9 to 11.0 nm for Fe/C and from 13.0 to 20.6 nm for Fe/NC-3.7). Their XRD patterns (Figure S6 of the SI) further show that the bulk Fe particles mostly remained in the metallic α-Fe phase with the (110) crystal plane (2θ = 44.6°) prevailing over the others (e.g., the (220) and (221) planes at 2θ values of 65.0° and 82.3°, respectively), while a small peak (2θ = 42.8°) ascribable to Fe_2C appeared in the more stable Fe/NC-3.7 catalyst. These data enable us to exclude the possibility of metal particle aggregation, carbon deposition, or the change of exposed crystal planes as predominant factors in affecting the catalyst stability. Instead, surface oxidation by the H_2O formed during the hydrodeoxygenation of *m*-cresol has been widely accepted as the main reason for the deactivation of Fe-based catalysts.[14] Accordingly, H_2O (0.5 kPa) was fed to the Fe/C and Fe/NC-3.7 catalysts and subjected to the same reaction conditions (40 kPa H_2, 350 °C) for 1 h so as to compare their oxidation resistance. Figure 7a shows that a H_2 consumption peak centered at 373 °C, which appears in the H_2-TPR process of the vapor-pretreated Fe/C catalyst but

https://dx.doi.org/10.1021/acscatal.0c00626
ACS Catal. 2020, 10, 7884−7893

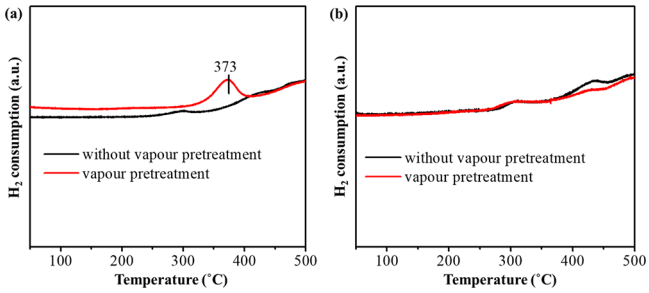

Figure 7. Effects of vapor pretreatment on the H_2-TPR profiles of (a) Fe/C and (b) Fe/NC-3.7 samples. Vapor pretreatment conditions: 0.5 kPa H_2O, 40 kPa H_2, balanced by N_2, 350 °C, 1 h.

does not appear in the catalyst without the vapor treatment. In contrast, the H_2-TPR profiles for the Fe/NC-3.7 catalysts with and without the vapor treatment are nearly identical (Figure 7b). These data clearly demonstrate that nitrogen doping of the carbon support catalysts improves the oxidation resistance of iron, consistent with the decrease of the oxygen affinity as conferred by the interaction between the Fe particles and the doped nitrogen sites (Figure 5).

We further compared the relative loss of *m*-cresol conversion rates after 10 h of time-on-stream for the Fe/NC-*x* samples and corresponding k_d values. As shown in Figure 8, the

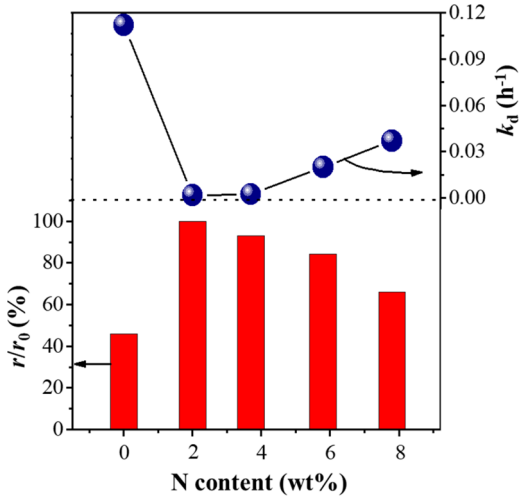

Figure 8. Relative rates with respect to the initial rates (r/r_0) for *m*-cresol conversion on Fe/NC-*x* catalysts after 10 h of time-on-stream at 350 °C and corresponding deactivation kinetic constants (k_d) as a function of N content. Reaction conditions: catalyst amount was varied to obtain an initial *m*-cresol conversion of ~20%, 0.5 kPa $P_{m\text{-cresol}}$, 40 kPa P_{H2}, balanced by N_2.

introduction of nitrogen into the carbon support resulted in a general improvement of the catalyst stability, but the relative activity loss of these Fe-based catalysts gradually increased from 0.9% to 36.8% as the N doping content increased from 2.0% to 7.8%, in agreement with the trend of the k_d values. It appears that a moderate nitrogen content is required to efficiently mitigate the oxidative deactivation of the Fe/C catalysts during hydrodeoxygenation reactions. It is also noteworthy that the initial turnover rates of the Fe/NC-*x* and Fe/C catalysts (calculated based on the surface Fe site densities measured from the H_2-TPR profiles of Figure 5) are proportional to the corresponding k_d values (Figure S7), indicating that the Fe catalysts that do not bind oxygen favorably are less active in hydrodeoxygenation reactions. Experimental and theoretical evidence are provided next to show that this effect of nitrogen content results from the various nitrogen species formed at different nitrogen contents.

3.4. Requirement of N Species for Stabilization of Fe/NC-*x* Catalysts. XPS characterization indicates that five kinds of nitrogen species may exist on the surface of the Fe/NC-*x* catalysts, including pyridinic, pyrrolic, graphitic, oxidic and amino functionalities (Figure 9a), which are distinguished by

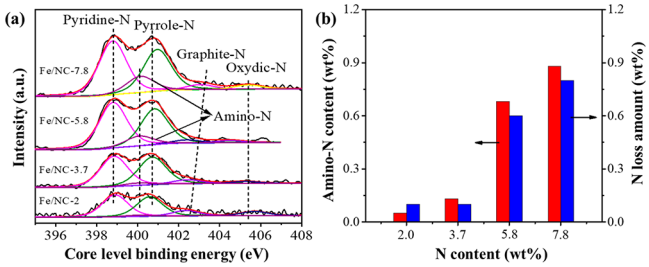

Figure 9. (a) N 1s XPS spectra of the Fe/NC-*x* samples and (b) corresponding amino-N content and N loss amount after 10 h of time-on-stream for these samples.

their core level binding energies.[41,42] In particular, pyridinic and pyrrolic nitrogen sites are the main species embedded in the carbon skeleton, with their binding energies of 398.8 and 400.5 eV, respectively. The XPS peak appearing at 402.3 eV is assigned to a mixture of graphitic and protonated N species (collectively called graphite-N), such as quaternary nitrogen and protonated pyridine, whereas the peaks appearing at 400.0 and 405.1 eV are ascribed to amine and nitro species on the carbon support surface, respectively.[43]

The relative surface concentration of these nitrogen moieties for the Fe/NC-*x* catalysts were quantitatively estimated by deconvoluting the multiple peaks in the XPS spectra (Figure 9a; detailed data shown in Table S4 of the SI). We noticed that the relative content of the aminic species increased from 0.05% to 0.88% in mass as the doped nitrogen concentration rose from 2.0% to 7.8% (Figure 9b). Moreover, the XPS spectra for the spent Fe/NC-*x* catalysts showed that amino species were significantly lost after 10 h of time-on-stream (Figure S8 of the SI), and the nitrogen lost by spent Fe/NC-*x* catalysts correlated well with the initial content of the amino species (Figure 9b). This data led us to conclude that the amino species may account for the weaker stability of the Fe/NC-*x* (x > 2.0%) catalysts with the higher nitrogen contents, because this high-content-preferred nitrogen species is much more unstable than the other surface nitrogen species under high-temperature reaction conditions.

In order to further examine the role of the amino species, amino groups were intentionally grafted on the surface of the pure carbon support via pretreatment with ammonium hydroxide. XPS spectra for the Fe particles supported on this amino-grafted carbon material (denoted as Fe/C-NH_3) confirmed the predominance of the aminic moieties among the surface nitrogen species of Fe/C-NH_3, whereas a negligible signal of N 1s was observed for the Fe/C catalyst without the ammonium hydroxide pretreatment (Figure 10a). As found for Fe/NC-*x*, the deactivation of Fe/C-NH_3 during the *m*-cresol hydrodeoxygenation reaction also followed the pseudo-first-order deactivation kinetics (Figure 10b). The measured k_d

https://dx.doi.org/10.1021/acscatal.0c00626
ACS Catal. 2020, 10, 7884−7893

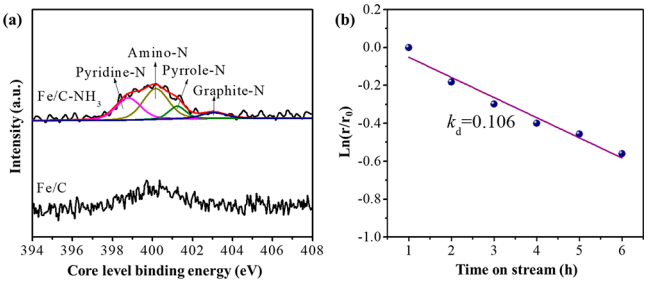

Figure 10. (a) N 1s XPS spectra for the Fe/C and Fe/C-NH_3 samples and (b) the pseudo-first-order deactivation kinetics of Fe/C-NH_3 during *m*-cresol hydrodeoxygenation (350 °C, 0.5 kPa *m*-cresol, 40 kPa H_2, balanced by N_2).

value for Fe/NC-NH_3 (0.106 h^{-1}) is much larger than those for the Fe/NC-*x* samples (<0.05 h^{-1}, Figure 8). This high instability of Fe/NC-NH_3 and the significant decrease of the amino concentration for this sample (from 46.0% to 37.0% after 10 h reaction, shown in Table S5 of the SI) agree well with our hypothesis on the negative effect of this thermally unstable amino specie in stabilizing the Fe/NC-*x* catalysts against oxidation. In other words, skeletal nitrogen sites, such as pyridine and pyrrole species, are crucial for efficient stabilization of the Fe/NC-*x* catalysts in hydrodeoxygenation reactions.

3.5. Computational Investigation of Fe Site Stability.

To better understand the effect of nitrogen functionality on catalyst durability, we computationally quantified the stability of Fe centers supported by various types of nitrogen functional groups (e.g., the pyridinic, pyrrolic, and aminic moieties) in the presence and in the absence of oxygen. It is noteworthy that the Fe−N electronic interaction between the Fe particles and the surface N sites of the carbon support appears to be mainly localized to the Fe atoms directly bound to the N sites, due to the low concentration of the surface N species (2.0−7.8 wt %) and the relatively large size of the Fe particles (10−20 nm). Although the number of these N-bound Fe centers is limited, they could still be effective in improving the oxidation resistance of the entire Fe nanoparticle. We postulate that the weakened oxygen affinity of these Fe centers, brought forth by the electronic interaction with the surface N species, renders them available for dissociating H_2 reactants to yield active H atoms during the hydrodeoxygenation reaction, which can diffuse along the entire surface of the Fe nanoparticle and scavenge the strongly bound O species via the formation of H_2O. Otherwise, the surface of the Fe nanoparticle will be oxidized by the O species (derived form *m*-cresol or H_2O), resulting in fast deactivation as observed for the Fe/C catalyst (Figure 6). This phenomenon of the small amount of N-modified Fe atoms in of providing the antioxidation stability of the whole Fe nanoparticle resembles the case of doping a noble metal on an Fe-based catalyst,[15] in which the active H atoms formed from H_2 dissociation on the noble metal sites can spill over onto the Fe surfaces, and even a ppm-level surface decoration of a noble metal can significantly enhance the catalyst stability in hydrodeoxygenation reactions. Because of the localized electronic effects of directly bound N on the Fe center that will be unaffected by the size of the Fe particles or the oxygenate feedstock, the following computational treatments used a single Fe atom as the probe to assess the interaction of the Fe center with various types of surface N species. This simple probe was proven to be adequate for our research target, as reflected from the excellent agreement between theory and experiment as shown below. These results indicate charge withdrawal plays a key role in site favorability, which is mediated by sterics and nitrogen functionality.

As depicted in Figure 11a−c, the nitrogen species that binds to Fe affects the binding energy (eq 1). While none of the edge

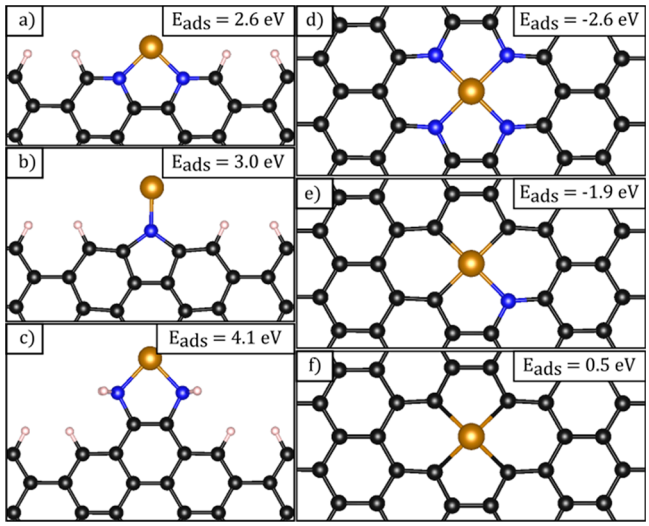

Figure 11. Comparison of Fe adsorption energies for pyridinic (a), pyrrolic (b), and aminic (c) edge sites and those for a graphene divacancy with increasing the pyridinic functionality (d−f). The sphere legend is as given in Figure 1.

sites shown here binds Fe favorably, they represent the only feasible configuration for amino groups and thus are used for reference. A comparison of the most favorable edge sites for each moiety reveals skeletal groups (e.g., pyridine and pyrrole) show less unfavorable binding energies than those of aminic groups by above 1.1 eV. Figure 11d−f further explores this trend, illustrating the effect of increasing pyridinic nitrogen content on the stability of Fe within a divacancy, where the incorporation of Fe becomes energetically favorable (since the adsorption energies are negative). It can be seen that the binding energy of Fe becomes increasingly favorable as it is surrounded by more pyridinic nitrogen atoms. A similar effect is also found for pyrroles, indicating that ideal sites are marked by a surrounding cluster of conjugated nitrogen groups with which the Fe particles can bond. The main difference between the pyrrolic functional groups and the pyridinic functional groups is that four pyridinic functional groups are needed to stabilize the Fe while Fe is stabilized with only three pyrrolic functional groups (see Table S6).

As revealed from the Bader charge analysis[43−45] for the bound Fe atoms (Figure 12a), this combination of sterics and nitrogen functionality allows the substrate to better interact with the Fe electronically, withdrawing charge and adsorbing more favorably to the N-doped graphene substrate. It can be seen that increasing the oxidation state of the bound Fe results in lower Fe adsorption energies and higher (i.e., less stable) oxidation energies (eq 2) for the resulting Fe compounds. Smooth trends are observed for both of the calculated energies (Figure 12; detailed data and structures shown in Tables S5−S7 of the SI), regardless of the graphene defect type (sheet or edge) and the nitrogen functionality. These theoretical data show all edge sites tested to be unfavorable, with the amino groups almost totally incapable of withdrawing charge. Internal

https://dx.doi.org/10.1021/acscatal.0c00626
ACS Catal. 2020, 10, 7884−7893

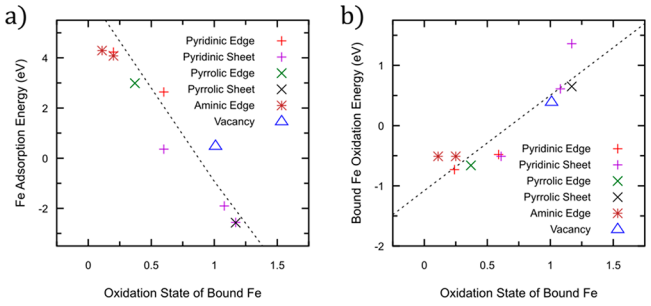

Figure 12. Comparisons of (a) the Fe adsorption energy in N-doped carbon and (b) the corresponding oxidation energies versus the Fe oxidation state.

graphene defects, on the other hand, can shield Fe from oxidation (Figure 12b) even in the case of a simple graphene divacancy (Figure 11f). Much better results are obtained by conjugated nitrogen groups (i.e., pyridinic and pyrrolic moieties), while amino groups are only feasible as edge sites and cause bound Fe to be practically metallic. This is consistent with the above experimental results showing skeletal nitrogen to produce more robust catalysts, while aminic functionalities readily result in deactivation under hydrodeoxygenation reaction conditions.

4. CONCLUSIONS

Fe/NC-*x* catalysts were successfully prepared with varying doped-N concentrations ranging from 2.0 to 7.8 wt %, and the effects on the stability and its mechanism toward N species were studied both experimentally and theoretically. XRD and TEM results demonstrate that the Fe particle size is regulated by the N density, with higher N content inducing a decrease in size via Fe-N interactions during catalyst deposition. H_2-TPR profiles with N_2O pretreatment and theoretical calculations further prove that the presence of N species can weaken the oxygen affinity of Fe, reflecting that the doped N sites affect the local electron density of the adsorbed Fe species significantly. With these N-induced synergistic effects, the representative Fe/NC-3.7 sample exhibits preferable reaction stability and antioxidation ability to water vapor as compared to Fe/C-based catalysts, which are verified by the *m*-cresol hydrodeoxygenation reaction and water vapor pretreated H_2-TPR experiments, respectively. Both controlled experiments and theoretical calculations further reveal that skeleton N species, especially the pyridine and pyrrole functional groups, play important roles in promoting Fe stability, and in reverse the amino-N species shows the poor function in the catalyst survivability for their wastage during hydrodeoxygenation.

■ ASSOCIATED CONTENT

Supporting Information

The Supporting Information is available free of charge at https://pubs.acs.org/doi/10.1021/acscatal.0c00626.

Nitrogen adsorption and desorption isotherms and texture properties of NC-*x* supports; Fe_2O_3 particle sizes of Fe_2O_3/NC-*x* samples; XRD patterns of reduced Fe/NC-*x* catalysts; TEM image and Fe particle size distribution for 10 wt % Fe/C; detailed products distribution of *m*-cresol hydrodeoxygenation; TEM and XRD profiles for the spent Fe-based catalysts; correlation between initial turnover rates and deactivation kinetic constants for Fe-based catalysts; N 1s XPS spectra of spent Fe/NC-*x* samples; XPS-determined surface N-containing species of the Fe/NC-*x* and Fe/C-NH_3 catalysts; structures of single-site Fe models applied in the theoretical calculations and corresponding DFT-derived adsorption and oxidation energies for bound Fe atoms (PDF)

■ AUTHOR INFORMATION

Corresponding Authors

Shuai Wang − *State Key Laboratory of Physical Chemistry of Solid Surfaces, Collaborative Innovation Center of Chemistry for Energy Materials, National Engineering Laboratory for Green Chemical Productions of Alcohols-Ethers-Esters, and College of Chemistry and Chemical Engineering, Xiamen University, Xiamen 361005, China;* orcid.org/0000-0002-4618-4162; Email: shuaiwang@xmu.edu.cn

Yong Wang − *Voiland School of Chemical Engineering and Bioengineering, Washington State University, Pullman, Washington 99164, United States;* orcid.org/0000-0002-8460-7410; Email: yongwang@pnnl.gov

Authors

Yanling Yang − *State Key Laboratory of Physical Chemistry of Solid Surfaces, Collaborative Innovation Center of Chemistry for Energy Materials, National Engineering Laboratory for Green Chemical Productions of Alcohols-Ethers-Esters, and College of Chemistry and Chemical Engineering, Xiamen University, Xiamen 361005, China*

Mingwu Tan − *State Key Laboratory of Physical Chemistry of Solid Surfaces, Collaborative Innovation Center of Chemistry for Energy Materials, National Engineering Laboratory for Green Chemical Productions of Alcohols-Ethers-Esters, and College of Chemistry and Chemical Engineering, Xiamen University, Xiamen 361005, China;* orcid.org/0000-0002-5099-7190

Aidan Garcia − *Voiland School of Chemical Engineering and Bioengineering, Washington State University, Pullman, Washington 99164, United States*

Zhaoxia Zhang − *State Key Laboratory of Physical Chemistry of Solid Surfaces, Collaborative Innovation Center of Chemistry for Energy Materials, National Engineering Laboratory for Green Chemical Productions of Alcohols-Ethers-Esters, and College of Chemistry and Chemical Engineering, Xiamen University, Xiamen 361005, China*

Jingdong Lin − *State Key Laboratory of Physical Chemistry of Solid Surfaces, Collaborative Innovation Center of Chemistry for Energy Materials, National Engineering Laboratory for Green Chemical Productions of Alcohols-Ethers-Esters, and College of Chemistry and Chemical Engineering, Xiamen University, Xiamen 361005, China;* orcid.org/0000-0003-0686-6908

Shaolong Wan − *State Key Laboratory of Physical Chemistry of Solid Surfaces, Collaborative Innovation Center of Chemistry for Energy Materials, National Engineering Laboratory for Green Chemical Productions of Alcohols-Ethers-Esters, and College of Chemistry and Chemical Engineering, Xiamen University, Xiamen 361005, China*

Jean-Sabin McEwen − *Voiland School of Chemical Engineering and Bioengineering, Department of Physics and Astronomy, Department of Chemistry, and Department of Biological Systems Engineering, Washington State University, Pullman, Washington 99164, United States; Institute for Integrated Catalysis, Pacific Northwest National Laboratory, Richland, Washington 99352, United States;* orcid.org/0000-0003-0931-4869

https://dx.doi.org/10.1021/acscatal.0c00626
ACS Catal. 2020, 10, 7884−7893

Complete contact information is available at:
https://pubs.acs.org/10.1021/acscatal.0c00626

Notes

The authors declare no competing financial interest.

■ ACKNOWLEDGMENTS

This work was supported by the National Natural Science Foundation of China (Nos. 21922201, 21872113, and 91545114) and the Fundamental Research Funds for the Central Universities (No. 20720190036). J.-S.M. and A.G. were supported by the National Science Foundation under Contract No. CBET-1703052. This research used resources from the Center for Institutional Research Computing at Washington State University. PNNL is a multiprogram national laboratory operated for the US DOE by Battelle.

■ REFERENCES

(1) Ragauskas, A. J.; Williams, C. K.; Davison, B. H.; Britovsek, G.; Cairney, J.; Eckert, C. A.; Frederick, W. J.; Hallett, J. P.; Leak, D. J.; Liotta, C. L.; Mielenz, J. R.; Murphy, R.; Templer, R.; Tschaplinski, T. The path forward for biofuels and biomaterials. *Science* **2006**, *311*, 484−489.
(2) Mohan, D.; Pittman, C. U., Jr.; Steele, P. H. Pyrolysis of wood/biomass for bio-oil: a critical review. *Energy Fuels* **2006**, *20*, 848−889.
(3) Huber, G. W.; Iborra, S.; Corma, A. Synthesis of transportation fuels from biomass: chemistry, catalysts, and engineering. *Chem. Rev.* **2006**, *106*, 4044−4098.
(4) Schutyser, W.; Renders, T.; Van den Bosch, S.; Koelewijn, S.-F.; Beckham, G. T.; Sels, B. F. Chemicals from lignin: an interplay of lignocellulose fractionation, depolymerisation, and upgrading. *Chem. Soc. Rev.* **2018**, *47*, 852−908.
(5) Sun, Z.; Fridrich, B.; de Santi, A.; Elangovan, S.; Barta, K. Bright side of lignin depolymerization: toward new platform chemicals. *Chem. Rev.* **2018**, *118*, 614−678.
(6) Liu, C.; Wang, H.; Karim, A. M.; Sun, J.; Wang, Y. Catalytic fast pyrolysis of lignocellulosic biomass. *Chem. Soc. Rev.* **2014**, *43*, 7594−7623.
(7) Pham, T. N.; Sooknoi, T.; Crossley, S. P.; Resasco, D. E. Ketonization of carboxylic acids: mechanisms, catalysts, and implications for biomass conversion. *ACS Catal.* **2013**, *3*, 2456−2473.
(8) Lin, Z.; Chen, R.; Qu, Z.; Chen, J. G. Hydrodeoxygenation of biomass-derived oxygenates over metal carbides: from model surfaces to powder catalysts. *Green Chem.* **2018**, *20*, 2679−2696.
(9) Hong, Y.; Hensley, A.; McEwen, J.-S.; Wang, Y. Perspective on catalytic hydrodeoxygenation of biomass pyrolysis oils: essential roles of Fe-based catalysts. *Catal. Lett.* **2016**, *146*, 1621−1633.
(10) Olcese, R. N.; Bettahar, M.; Petitjean, D.; Malaman, B.; Giovanella, F.; Dufour, A. Gas-phase hydrodeoxygenation of Guaiacol over Fe/SiO_2 catalyst. *Appl. Catal., B* **2012**, *115*−*116*, 63−73.
(11) Sun, J.; Karim, A. M.; Zhang, H.; Kovarik, L.; Li, X. S.; Hensley, A. J.; McEwen, J.-S.; Wang, Y. Carbon-supported bimetallic Pd−Fe catalysts for vapor-phase hydrodeoxygenation of guaiacol. *J. Catal.* **2013**, *306*, 47−57.
(12) Sun, J.; Karim, A. M.; Li, X. S.; Rainbolt, J.; Kovarik, L.; Shin, Y.; Wang, Y. Hierarchically structured catalysts for cascade and selective steam reforming/hydrodeoxygenation reactions. *Chem. Commun.* **2015**, *51*, 16617−16620.
(13) Hong, Y.; Zhang, H.; Sun, J.; Ayman, K. M.; Hensley, A. J. R.; Gu, M.; Engelhard, M. H.; McEwen, J.-S.; Wang, Y. Synergistic catalysis between Pd and Fe in gas phase hydrodeoxygenation of *m*-cresol. *ACS Catal.* **2014**, *4*, 3335−3345.
(14) Hong, Y.; Zhang, S.; Tao, F. F.; Wang, Y. Stabilization of iron-based catalysts against oxidation: an in situ ambient-pressure X-ray photoelectron spectroscopy (AP-XPS) study. *ACS Catal.* **2017**, *7*, 3639−3643.
(15) Yang, Y.; Chen, J.; Zhang, L.; Tan, M.; Lin, J.; Wan, S.; Wang, S.; Wang, Y. Enhanced antioxidation stability of iron-based catalysts via surface decoration with ppm platinum. *ACS Sustain. Chem. Eng.* **2018**, *6*, 14010−14016.
(16) Ren, H.; Wang, Y.; Yang, Y.; Tang, X.; Peng, Y.; Peng, H.; Xiao, L.; Lu, J.; Abruña, H. D.; Zhuang, L. Fe/N/C nanotubes with atomic Fe sites: a highly active cathode catalyst for alkaline polymer electrolyte fuel cells. *ACS Catal.* **2017**, *7*, 6485−6492.
(17) Tang, F.; Lei, H.; Wang, S.; Wang, H.; Jin, Z. A novel Fe-N-C catalyst for efficient oxygen reduction reaction based on polydopamine nanotubes. *Nanoscale* **2017**, *9*, 17364−17370.
(18) Zhang, H.; Hwang, S.; Wang, M.; Feng, Z.; Karakalos, S.; Luo, L.; Qiao, Z.; Xie, X.; Wang, C.; Su, D.; Shao, Y.; Wu, G. Single atomic iron catalysts for oxygen reduction in acidic media: particle size control and thermal activation. *J. Am. Chem. Soc.* **2017**, *139*, 14143−14149.
(19) Jiang, W. J.; Gu, L.; Li, L.; Zhang, Y.; Zhang, X.; Zhang, L. J.; Wang, J. Q.; Hu, J. S.; Wei, Z.; Wan, L. J. Understanding the high activity of Fe-N-C electrocatalysts in oxygen reduction: Fe/Fe_3C nanoparticles boost the activity of Fe-N_x. *J. Am. Chem. Soc.* **2016**, *138*, 3570−3578.
(20) Ju, W.; Bagger, A.; Hao, G.-P.; Varela, A. S.; Sinev, I.; Bon, V.; Roldan Cuenya, B.; Kaskel, S.; Rossmeisl, J.; Strasser, P. Understanding activity and selectivity of metal-nitrogen-doped carbon catalysts for electrochemical reduction of CO_2. *Nat. Commun.* **2017**, *8*, 944.
(21) Liu, W.; Zhang, L.; Liu, X.; Liu, X.; Yang, X.; Miao, S.; Wang, W.; Wang, A.; Zhang, T. Discriminating catalytically active FeN_x species of atomically dispersed Fe-N-C catalyst for selective oxidation of the C-H Bond. *J. Am. Chem. Soc.* **2017**, *139*, 10790−10798.
(22) Chen, X.; Deng, D.; Pan, X.; Hu, Y.; Bao, X. N-doped graphene as an electron donor of iron catalysts for CO hydrogenation to light olefins. *Chem. Commun.* **2015**, *51*, 217−220.
(23) Zhang, R.; McEwen, J.-S. Local environment sensitivity of the Cu K-edge XANES features in Cu-SSZ-13: analysis from first-principles. *J. Phys. Chem. Lett.* **2018**, *9*, 3035−3042.
(24) Zhang, R.; Li, H.; McEwen, J.-S. Chemical sensitivity of valence-to-core X-ray emission spectroscopy due to the ligand and the oxidation state: a computational study on Cu-SSZ-13 with multiple H_2O and NH_3 adsorption. *J. Phys. Chem. C* **2017**, *121*, 25759−25767.
(25) Li, M.; Tang, M.; Deng, J.; Wang, Y. Nitrogen-doped flower-like porous carbon materials directed by in situ hydrolysed MgO: promising support for Ru nanoparticles in catalytic hydrogenations. *Nano Res.* **2016**, *9*, 3129−3140.
(26) Kresse, G.; Hafner, J. Ab initio molecular dynamics for liquid metals. *Phys. Rev. B: Condens. Matter Mater. Phys.* **1993**, *47*, 558−561.
(27) Kresse, G.; Furthmüller, J. Efficient iterative schemes for ab initio total-energy calculations using a plane-wave basis set. *Phys. Rev. B: Condens. Matter Mater. Phys.* **1996**, *54*, 11169−11186.
(28) Kresse, G.; Joubert, D. From ultrasoft pseudopotentials to the projector augmented-wave method. *Phys. Rev. B: Condens. Matter Mater. Phys.* **1999**, *59*, 1758−1775.
(29) Perdew, J. P.; Burke, K.; Ernzerhof, M. Generalized gradient approximation made simple. *Phys. Rev. Lett.* **1996**, *77*, 3865−3868.
(30) Perdew, J. P.; Burke, K.; Ernzerhof, M. Generalized gradient approximation made simple [Phys. Rev. Lett. 77, 3865 (1996)]. *Phys. Rev. Lett.* **1997**, *78*, 1396−1396.
(31) Ayiania, M.; Hensley, A. J. R.; Groden, K.; Garcia-Perez, M.; McEwen, J.-S. Thermodynamic stability of nitrogen functionalities and defects in graphene and graphene nanoribbons from first principles. *Carbon* **2019**, *152*, 715−726.
(32) Monkhorst, H. J.; Pack, J. D. Special points for Brillouin-zone integrations. *Phys. Rev. B* **1976**, *13*, 5188−5192.
(33) Pan, F.; Li, B.; Deng, W.; Du, Z.; Gang, Y.; Wang, G.; Li, Y. Promoting electrocatalytic CO_2 reduction on nitrogen-doped carbon with sulfur addition. *Appl. Catal., B* **2019**, *252*, 240−249.
(34) Gao, Y.; Li, T.; Zhu, Y.; Chen, Z.; Liang, J.; Zeng, Q.; Lyu, L.; Hu, C. Highly nitrogen-doped porous carbon transformed from

graphitic carbon nitride for efficient metal-free catalysis. *J. Hazard. Mater.* **2020**, *393*, 121280.
(35) Zhang, Z.; Zhang, C.; Sun, J.; Kou, T.; Bai, Q.; Wang, Y.; Ding, Y. Ultrafine nanoporous PdFe/Fe_3O_4 catalysts with doubly enhanced activities towards electro-oxidation of methanol and ethanol in alkaline media. *J. Mater. Chem. A* **2013**, *1*, 3620−3628.
(36) Liu, X.; Xu, L.; Xu, G.; Jia, W.; Ma, Y.; Zhang, Y. Selective hydrodeoxygenation of lignin-derived phenols to cyclohexanols or cyclohexanes over magnetic CoN_x@NC catalysts under mild conditions. *ACS Catal.* **2016**, *6*, 7611−7620.
(37) Yang, F.; Liu, D.; Zhao, Y.; Wang, H.; Han, J.; Ge, Q.; Zhu, X. Size dependence of vapor phase hydrodeoxygenation of *m*-cresol on Ni/SiO_2 catalysts. *ACS Catal.* **2018**, *8*, 1672−1682.
(38) Hensley, A. J. R.; Hong, Y.; Zhang, R.; Zhang, H.; Sun, J.; Wang, Y.; McEwen, J.-S. Enhanced Fe_2O_3 reducibility via surface modification with Pd: characterizing the synergy within Pd/Fe catalysts for hydrodeoxygenation reactions. *ACS Catal.* **2014**, *4*, 3381−3392.
(39) Wu, C. T.; Yu, K. M.; Liao, F.; Young, N.; Nellist, P.; Dent, A.; Kroner, A.; Tsang, S. C. A non-syn-gas catalytic route to methanol production. *Nat. Commun.* **2012**, *3*, 1050.
(40) Sirous Rezaei, P.; Shafaghat, H.; Daud, W. M. A. W. Origin of catalyst deactivation in atmospheric hydrogenolysis of *m*-cresol over Fe/HBeta. *RSC Adv.* **2015**, *5*, 51278−51285.
(41) Chen, Y.; Gokhale, R.; Serov, A.; Artyushkova, K.; Atanassov, P. Novel highly active and selective Fe-N-C oxygen reduction electrocatalysts derived from in-situ polymerization pyrolysis. *Nano Energy* **2017**, *38*, 201−209.
(42) Wei, H.; Qian, W.; Fu, N.; Chen, H.; Liu, J.; Jiang, X.; Lan, G.; Lin, H.; Han, S. Facile synthesis of nitrogen-doped porous carbons for CO_2 capture and supercapacitors. *J. Mater. Sci.* **2017**, *52*, 10308−10320.
(43) Kabir, S.; Artyushkova, K.; Serov, A.; Atanassov, P. Role of nitrogen moieties in N-doped 3D-graphene nanosheets for oxygen electroreduction in acidic and alkaline media. *ACS Appl. Mater. Interfaces* **2018**, *10*, 11623−11632.
(44) Tang, W.; Sanville, E.; Henkelman, G. A grid-based Bader analysis algorithm without lattice bias. *J. Phys.: Condens. Matter* **2009**, *21*, 084204.
(45) Yu, M.; Trinkle, D. R. Accurate and efficient algorithm for Bader charge integration. *J. Chem. Phys.* **2011**, *134*, 064111.

https://dx.doi.org/10.1021/acscatal.0c00626
ACS Catal. 2020, 10, 7884−7893